Talanta 81 (2010) 1045–1055

Contents lists available at ScienceDirect

Talanta

journal homepage: www.elsevier.com/locate/talanta

Probing the electrochemical double layer of an ionic liquid using voltammetry and impedance spectroscopy: A comparative study of carbon nanotube and glassy carbon electrodes in $[EMIM]^+[EtSO_4]^-$

J.P. Zheng[a], P.C. Goonetilleke[a], C.M. Pettit[b], D. Roy[a,*]

[a] Department of Physics, Clarkson University, Clarkson Ave, Potsdam, NY 13699-5820, USA
[b] Department of Physics, Emporia State University, Emporia, KS 66801-5087, USA

ARTICLE INFO

Article history:
Received 21 December 2009
Received in revised form 25 January 2010
Accepted 27 January 2010
Available online 4 February 2010

Keywords:
Carbon nanotube
Cyclic voltammetry
Double layer capacitance
Glassy carbon
Impedance spectroscopy
Ionic liquid

ABSTRACT

Cyclic voltammetry (CV) and electrochemical impedance spectroscopy (EIS) are compared as techniques for analyzing double layer capacitances of ionic liquids (ILs) at the surfaces of two carbon-based electrodes. These systems are relevant for energy storage supercapacitors and often are associated with unconventional electrochemical properties. Certain theoretical and experimental aspects of CV and EIS necessary for quantitative evaluation of the capacitance characteristics of such systems are explored. The experiments use 1-ethyl-3-methyl imidazolium ethylsulfate as a model IL electrolyte in combination with a porous electrode of carbon nanotubes (CNTs). The results are compared with those obtained with a nonporous glassy carbon (GC) electrode. The time is constant, and hence the power delivery characteristics of the experimental cell are affected by the electrolyte resistance and residual faradaic reactions of the IL, as well as by the spatially inhomogeneous electrode surfaces. It is shown that adequate characterization of these IL–electrode systems can be achieved by combining CV with EIS. A phenomenological framework for utilizing this combination is discussed.

1. Introduction

Room temperature ionic liquid (IL) electrolytes and carbon nanotube (CNT) electrodes are promising components of electrochemical supercapacitors for renewable energy storage [1–4]. New technological developments involving these systems currently rely on adequate characterization of the rather non-traditional electrochemical properties of IL–CNT interfaces [5–8]. The techniques of direct current (D.C.) cyclic voltammetry (CV) and alternating current (A.C.) electrochemical impedance spectroscopy (EIS) are commonly used for such characterization studies [8]. However, the traditional frameworks of these techniques often are not sufficient to fully support quantitative analyses of experimental data for these relatively complex systems. For instance, the classical approach to double layer capacitance measurements heavily centers on spatially homogeneous, ideally polarized electrode (IPE) systems that often are restricted to Hg electrodes of well-defined, flat and strictly nonfaradaic interfaces in aqueous electrolytes [8,10–15]. Frequently, these traditional formalisms of CV and EIS do not apply to IL–CNT systems that are associated with non-negligible solution resistances, large interfacial capacitances, faradaic side reactions and highly inhomogeneous (porous) surface morphologies [8,10–15].

In a recent publication, we have discussed certain aspects of the CV technique for studying capacitive behaviors of IL–CNT interfaces [8]. In the present work, we examine the utility of A.C. EIS for such studies, and using an exemplary system, present a side-by-side comparison of differential capacitance results obtained from CV and EIS. A non-halide IL of 1-ethyl-3-methyl imidazolium ethylsulfate ($[EMIM]^+[EtSO_4]^-$ or EMIM-$EtSO_4$) is used for this purpose in combination with a porous paper electrode of multiwall CNTs. The results for the CNT electrode are benchmarked against those obtained from a parallel set of measurements using a nonporous glassy carbon (GC) electrode.

The experiments reported here show that both the CNT and the GC electrodes in EMIM-$EtSO_4$ deviate from the ideal behavior of homogeneous IPEs, and that the analysis of CV and EIS data for these systems requires a relatively more generalized formalism. By using previously developed electrode equivalent circuit (EEC) models [10,14], we briefly review the theoretical framework necessary for such a formal approach. We also examine how the results of CV and EIS for typical IL–carbon interfaces may depend on the assumptions and simplifications incorporated in the models typically employed to process the raw data. The double layer capacitances, as well as the polarization resistances of faradaic leakage of the IL–electrode interfaces are compared using CV and EIS.

* Corresponding author. Tel.: +1 315 268 6676; fax: +1 315 268 6610.
E-mail address: samoy@clarkson.edu (D. Roy).

0039-9140/$ – see front matter © 2010 Elsevier B.V. All rights reserved.
doi:10.1016/j.talanta.2010.01.059

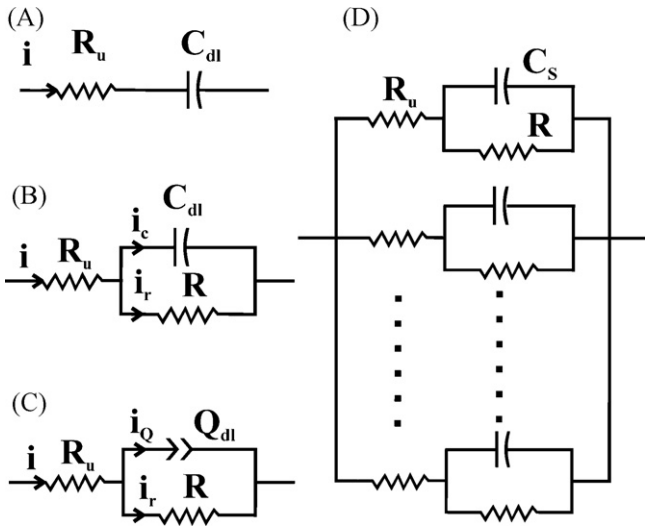

Fig. 1. Circuit models of IL–electrode interfaces used to describe the D.C. (A and B) and A.C. (C and D) electrochemical response characteristics of IL–electrode interfaces. (A) An EEC based on the assumptions of negligible faradic reactions ($R \gg R_u$) and frequency dispersion ($n = 1$). (B) A more generalized version of (A) with the inclusion of a faradaic reaction resistance R. (C) Further generalization of EEC (B), where C_{dl} is frequency-dispersed, detected as the CPE, Q_{dl}, in EIS experiments. (D) Brug et al.'s ladder-EEC model of a spatially inhomogeneous faradaically active electrode interface [14].

2. Theoretical considerations

2.1. Circuit models of ionic liquid interfaces at spatially inhomogeneous electrodes

For energy storage applications, the operating voltages of IL–electrode interfaces are kept within the "electrochemical window" of the system, where faradaic currents due to self-discharge of the double layer capacitor are minimal [3,5,16,17]. Ideally, variations in the double layer capacitance value (C_{dl}) of the system should also be small within this voltage range [1,4,18]. The CV and EIS characteristics of spatially homogeneous faradaically inactive interfaces often are described by the simple D.C. blocking EEC of Fig. 1A, where R_u denotes the uncompensated electrolyte resistance. In this case, the capacitance charge–discharge current (i_c) is equal to the total current (i) through the interface, and R_uC_{dl} is a characteristic time constant (τ_0) that determines how fast C_{dl} can be charged or discharged. This time constant dictates the power delivery characteristics of the double layer capacitor cell [19]. If the working electrode is flat and homogeneous, but associated with faradaic side reactions, the EEC of Fig. 1B can be used with the inclusion of a polarization (or charge transfer) resistance (R) in parallel with C_{dl} [20].

For rough and/or porous inhomogeneous electrodes, the frequency-dispersed capacitance C_{dl} typically takes the form of a constant phase element (CPE) Q_{dl} [11–15] in EIS, as shown in Fig. 1C. The current through the CPE is denoted as i_Q. IL double layers formed at the surfaces of carbon-based electrodes often match this circuit model of Fig. 1C [21,22], owing to the intrinsically inhomogeneous large areas of the porous electrodes used in such devices. The polarization resistance in these cases can arise from faradaically active impurities in the system [8,12].

The complex admittance $Y(Q_{dl})$ and impedance $Z(Q_{dl})$ of the CPE in Fig. 1C are expressed as [15,18]

$$Y(Q_{dl}) = [Z(Q_{dl})]^{-1} = Y_0(j\omega)^n, \quad (1)$$

where Y_0 is real and represents the frequency-independent part of $Y(Q_{dl})$; $j = \sqrt{-1}$; ω is the angular frequency of A.C. perturbation; n is a measure of electrode-surface roughness/in-homogeneity [11–14,23,24]; $0 \le n \le 1$. For $n = 1$, Y_0 acquires the unit of capacitance, leading to the identity, $Y_0 = C_{dl}$. If the electrode surface is inhomogeneous/rough but lacks faradaic activity, the polarization resistance can be neglected (left as an open branch) in Fig. 1C and the D.C. form of the resulting circuit would be the same as Fig. 1A. According to previous findings, the D.C. CV characteristics of the CNT-[EMIM-EtSO$_4$] interface can be satisfactorily described using the model shown in Fig. 1B, and C_{dl} can be determined from the CV data using this EEC [8]. Later in the present report, we show that CV of GC-[EMIM-EtSO$_4$] also follows the description of Fig. 1B, and that the EIS responses of both CNT and GC in EMIM-EtSO$_4$ correspond to the model in Fig. 1C. Thus, to obtain C_{dl} from EIS for these systems, we focus on the EEC in Fig. 1C [8,12,21,22].

The elements Y_0, R_u and R can be determined by fitting experimental EIS data to calculated impedance spectra for Fig. 1C using the complex nonlinear least square (CNLS) method [10]. Such a CNLS-analyzed EEC represents a site-averaged overall response of the electrode surface, where site-specific capacitance contributions of the inhomogeneous surface are lumped together (along with R_u and R) in Y_0 [12]. In other words, C_{dl} as well as both R_u and R are thus included in Y_0 [14,15] and as a result, CNLS calculations alone do not generally provide the value of C_{dl} in terms of Y_0.

To establish the relationship between Y_0 and C_{dl} (as well as R_u and R), it is necessary to "expand" the effective single-loop EEC of Fig. 1C, where the site-specific capacitance contributions can be explicitly included. Several transmission line models with varying levels of complexity have been proposed for this purpose [10], and a simple one due to Brug et al. [14] is shown here in Fig. 1D. In this un-branched ladder-EEC model, the impedance contribution of each electrochemically active surface site is described in terms of a sub-circuit having the basic form of Fig. 1B. A parallel combination of all the sub-circuits (assumed to be infinite in number) describing the full electrode surface is taken as the overall EEC in Fig. 1C. It is assumed that only the capacitance contribution of the electrode varies from site to site, with R_u and R having their same respective values across the electrode surface. This model has been considered in previous reports [15,25] and will be reviewed as well as utilized in the present work to illustrate the practical considerations relevant for EIS-based measurements of C_{dl} involving IL–electrode interfaces.

2.2. Considerations for D.C. cyclic voltammetry of CNT and GC electrodes in ionic liquid electrolytes

The D.C. current–voltage characteristics of the EEC of Fig. 1B have been discussed in Ref. [8], and the main equations are summarized below. In the mid-region of the electrochemical voltage window, the D.C. current (i) of CV has the form,

$$i = i_r \pm \nu_{dc}C'_{dl}, \quad (2)$$

where $\nu_{dc}C'_{dl} = i_c$, and ν_{dc} is the voltage scan speed; $\nu_{dc} = (dE/dt)$, with E denoting the applied D.C. voltage; C'_{dl} is a scaled capacitance; $C'_{dl} = (R_t/R_u)C_{dl}$, and $R_t = (R_uR)/(R_u + R)$. The time constant ($\tau_0 = R_uC_{dl}$) of the nonfaradaic electrode takes a new value, τ'_0, due to faradaic effects represented by R:

$$\tau'_0 = R_tC_{dl} = R_uC'_{dl} = \tau_0(\xi^{-1}), \quad (3)$$

where $\xi = 1 + (R_uR^{-1})$. If $R >> R_u$ (predominantly nonfaradaic case), $R \approx R_u$ then, and $\tau'_0 \approx \tau_0$.

Usually, R_u and R are independent of ν_{dc} and both R and i_r are functions of E. If i_r is affected by diffusion limited reactions, this current should be proportional to $\sqrt{\nu_{dc}}$ [8,10]. On the other hand, if i_r is kinetically controlled and not significantly affected by intermediate adsorbates, it should be independent of ν_{dc} in CV. In the latter case, according to Eq. (2), i varies linearly with ν_{dc}, yielding

slopes and intercepts given by C'_{dl} and i_r, respectively. If faradaic reactions are absent, then Fig. 1B simplifies to Fig. 1A, with $R \to \infty$ and $i_r \to 0$, so that $i \approx i_c$, and Eq. (2) then takes the simple form,

$$C_{dl} \approx i(\nu_{dc})^{-1}, \tag{4}$$

with $R_t \approx R_u$ and $C'_{dl} \approx C_{dl}$. In this special case, Eq. (4) provides a relatively simple method of determining C_{dl} directly from the CV data [26,27]. The validity of this approach for a given system can be checked by checking (i) if the experimental $i - \nu_{dc}$ graphs are linear, and (ii) if the intercepts of the linear plots on the current-axis are zero [8].

2.3. Determination of polarization resistance and double layer capacitance using CV

At voltages near the open circuit potential (OCP), i_r contains both anodic (i_{ra}) and cathodic (i_{rc}) contributions: $i = i_{ra} + i_{rc}$, where i_{rc} is negative. The polarization resistances associated with these individual currents are given as $R_a = (\partial i_{ra}/\partial E)^{-1}$ and $R_c = (\partial i_{rc}/\partial E)^{-1}$. Thus, although EIS does not directly show the composition of the net polarization resistance, the latter (defined as $R = (\partial i/\partial E)^{-1}$) effectively is a parallel combination of R_a and R_c: $(1/R) = (1/R_a) + (1/R_c)$ [8]. For $E \approx$ OCP, one has $|i_{ra}| \approx |i_{rc}|$, so that $R_a \approx R_c$, and then R simply represents an average of the anodic and cathodic polarization resistances. At large positive overpotentials i_{rc} is suppressed, resulting in very large values of R_c, so that $R(E >> \text{OCP}) \approx R_a$. Similarly, at large negative overpotentials, $R(E << \text{OCP}) \approx R_c$.

If Eq. (3) is operative instead of Eq. (4), then only the scaled capacitance C'_{dl} is directly obtainable from CV [8]. Conversion of C'_{dl} to C_{dl} requires evaluation of both R and R_u, and as discussed above, R can be determined using CV. However, measurement of R_u for ILs using CV [25] may not always be straightforward, especially if the kinetic equations of aqueous electrochemistry used for such analyses do not adequately apply to IL electrolytes [6]. On the other hand, EIS offers a direct and simple method of measuring R_u, which can be combined with D.C. CV to determine C_{dl} from C'_{dl} [28,29].

2.4. Considerations for A.C. impedance spectroscopy of CNT and GC electrodes in ionic liquid electrolytes

A key element of EIS experiments involving IL–carbon systems is the functional form of Y_0 in terms of R_u, R and C_{dl}, and Brug et al.'s ladder-EEC model [14], shown here in Fig. 1D, addresses this subject. However, this model is based on certain assumptions that are central to understanding both the general aspects and the limitations of conventional EIS-based measurements of C_{dl} for spatially inhomogeneous and faradaically active interfaces. Therefore, it is necessary to examine the underlying assumptions of the ladder model, as they provide the guidelines to determine the suitability of the experimental systems to be associated with this specific model. To do this, using Fig. 1D, we briefly review below the main steps of Brug et al.'s calculations, and note the system-requirements as specified in the ladder-EEC model.

The net admittance (Y_s) and the impedance (Z_s) of a given site-specific EEC sub-unit in Fig. 1D can be written as $Z_s = (Y_s)^{-1} = R_u + (Y_{sE})^{-1}$. The last expression is equivalent to writing

$$Y_s = \frac{1}{R_u}\left(1 - \frac{1}{1 + R_u Y_{sE}}\right), \tag{5}$$

where Y_{sE} is the effective admittance of the parallel combination of C_s and R_s at the surface site considered:

$$Y_{sE} = (R_s)^{-1} + j\omega C_s. \tag{6}$$

The parameter s can be continuously varied from $-\infty$ to $+\infty$ to include capacitance contributions of all surface sites. In addition to having its un-branched form, the simple ladder model also assumes negligible effects of diffusion. Thus, no diffusion elements are incorporated in Fig. 1D. Another assumption of this approach is that the resistance is same for all sites ($R_s \equiv R$), and that only C_s is site-dependent, having the form: $C_s = C_{dl}^{av} \exp(s)$. This C_{dl}^{av} is a site-averaged net double layer capacitance resulting from the combined contributions of all surface sites. According to this formulation [14], $\tau_s = R_u C_s$, or,

$$\tau_s = \tau_0[\exp(s)] = (\tau'_0)\xi \cdot \exp(s), \tag{7}$$

where τ_s represents a surface site-dependent time constant under nonfaradaic conditions ($R \gg R_u$). The term τ'_0 has the same form of Eq. (3), but in the context of EIS for distributed capacitance, we denote τ_0 of this equation slightly differently by writing $\tau_0 = R_u C_{dl}^{av}$. Eqs. (6) and (7) can be combined as: $R_u Y_{sE} = R_u R^{-1} + j\omega\tau_s$. Incorporation of the last expression in Eq. (5) gives:

$$Y_s = \frac{1}{R_u}\left[1 - \frac{1}{\xi\{1 + j\omega\tau'_0 \exp(s)\}}\right]. \tag{8}$$

Using Eq. (8), the site-averaged overall impedance (Y) of the electrode surface is written as

$$Y = \int_{-\infty}^{\infty} Y_s F(s) ds, \tag{9}$$

where $F(s)$ is a normalized distribution function.

The next assumption, necessary for further simplification of Eq. (9) in the ladder-EEC approach, involves adapting the following form of $F(s)$ [14]:

$$F(s) = \frac{(\pi^{-1})[\sin(1-n)\pi]}{\exp(ns) + \exp(-ns) - 2\cos[(1-n)\pi]}. \tag{10}$$

By using Eqs. (9) and (10) in Eq. (8), and integrating the resulting expression [14],

$$Y = \frac{1}{R_u}\left[1 - \frac{1}{\xi + (j\omega R_u C_{dl}^{av})^n (\xi)^{1-n}}\right]. \tag{11}$$

The capacitance C_{dl}^{av} is explicitly contained in Eq. (11).

In CNLS analysis of experimental EIS data, the distributed A.C. response of the EEC of Fig. 1D would be detected as a single-loop effective EEC as shown in Fig. 1C. According to Eq. (1), the total admittance (Y) of this EEC has the form:

$$Y = \frac{1}{R_u}\left[1 - \frac{1}{\xi + Y_0 R_u (j\omega)^n}\right] \tag{12}$$

A comparison of Eqs. (11) and (12) shows how the composite parameter Y_0 is related to C_{dl}^{av}, R_u and R [19]:

$$Y_0 = \left(\frac{\tau_0}{R_u}\right)^n \left(\frac{1}{R_u} + \frac{1}{R}\right)^{1-n} = \frac{(C_{dl}^{av})^n}{(R_t)^{1-n}}. \tag{13}$$

The term C_{dl}^{av} in Eq. (13) for A.C. EIS is equivalent to C_{dl} considered in Eqs. (2)–(4) for D.C. CV. Experimentally, however, depending on the system studied, the D.C.- and A.C.-measured values of this capacitance could be somewhat differently affected by the different measurement conditions of the two techniques [11,13,30–32]. For instance, time-domain response of the CPE [32,33], possibly activated at large values of ν_{dc}, could affect CV based evaluation of C_{dl} (via the measurement of i) to a different extent in comparison with the corresponding frequency-domain effects of EIS on C_{dl}^{av} [31–33]. The relative effects of these different measurement conditions would be determined by the detailed control variables used in the D.C. and the A.C. experiments [13,23]. To probe the presence of these differences between CV- and EIS-measured capacitances, we have introduced here two different notations for this parameter.

From the foregoing discussion, we summarize the following necessary features of the experimental systems that can be described using Eq (13): (i) the distributed impedance network of the interface is un-branched; (ii) the faradaic charge transfer step is slow (no diffusion effects) and uniform (same value of R) across all sites; (iii) R_u is site independent; (iv) the double layer capacitance is site-dependent, and can be described according to Eq. (7); (v) overall site-distribution of the interfacial admittance follows the phenomenological Eq. (10).

Several authors including Brug et al. [14] and others [10,15] have suggested various methods to generalize the basic ladder-EEC model, which could eliminate the need for adapting some of the aforementioned assumptions. However, to our knowledge, such generalized treatments have not been widely explored to study double layer capacitances of IL–carbon systems using the EIS approach. The simple un-branched ladder model, which leads to Eq. (13), is frequently cited in the literature, and will also be used here to examine how EIS results for double layer capacitances of the IL–CNT and IL–GC interfaces compare with the corresponding findings of CV.

2.5. Determination of polarization resistance and double layer capacitance using EIS

CNLS-calculated fits to experimental EIS data would provide the value of R, Y_0, n, and R_u considered in Fig. 1C. This would lead to the evaluation of C_{dl}^{av} from Eq. (13):

$$C_{dl}^{av} = [y_0(R_t)^{1-n}]^{1/n}. \quad (14)$$

Eq. (14) implies the identity, $C_{dl}^{av} = Y_0$, only empirically for $0.98 \le n \le 1$ [11]. In addition to the EIS method discussed above, single-frequency impedance techniques have also been used to measure double layer capacitances of IL–electrode systems [34–36]. To illustrate the essential elements of this latter approach, we consider the circuit impedance (Z) in Fig. 1C:

$$Z = R_u + \frac{R}{1 + Y_0 R(j\omega)^n}, \quad (15)$$

where $(j)^n = [\cos(n\pi/2) + j\sin(n\pi/2)]$ according to De-Moivre's theorem. Evaluating the imaginary component (Z'') of this Z, one obtains:

$$-\frac{1}{\omega Z''} = \frac{Y_0\omega^{n-1}}{\sin(n\pi/2)} + \frac{2}{\omega R}\cot(n\pi/2) + \frac{1}{R^2 Y_0 \omega^{1+n}\sin(n\pi/2)} \quad (16)$$

If the working electrode interface is strictly nonfaradaic ($R \to \infty$) and spatially homogeneous ($n = 1$), then $Y_0 \equiv C_{dl}^{av}$ and Eq. (16) simplifies to [28,34–36]:

$$C_{dl}^{av} \approx -(\omega Z'')^{-1} \quad (17)$$

The applicability of Eq. (17) to the presently used experimental systems will be tested here.

3. Experimental details

The surface of the flat GC electrode (BASi model MF-2012, 3.0 mm diameter) was polished on a Buehler Microcloth® using a paste of 0.05 μm alumina powder and triply distilled water [8]. The CNT electrode was assembled using multiwall (MW) CNT paper (obtained from Nanolab), affixed to a Teflon holder with electrical connection provided by Ag paste and a Cu current collector. SEM images of the MWCNT film provided by the manufacturer showed about 100 μm thick and 50% dense free-standing CNTs of approximately 40 nm average diameter. The CNT electrode contained 95.93% C, and its most predominant impurity was Fe (1.65%). For each working electrode, an active (geometric) surface area of 0.07 cm^2 was exposed to the experimental IL. Before each experiment, the thoroughly acetone-cleaned (and sonicated) electrodes were dried under an Ar stream, and the CNT sample was additionally dried overnight in a vacuum oven at 100 °C [37]. Both the GC and the CNT electrodes were soaked for ≥1 h in the IL electrolyte prior to all experiments, while the OCP of the system was allowed to stabilize.

EMIM-$EtSO_4$ ($C_8H_{16}N_2O_4S$), obtained from Solvent Innovation was used without further purification. The IL was kept in a vacuum oven at 80 °C temperature and −30 mm Hg pressure for 24 h and was bubbled with ultrahigh purity Ar for 1 h before using in electrochemical experiments. The experimental cell was controlled with a Solartron 1287A potentiostat/galvanostat, coupled with a model 1252A frequency response analyzer. All experiments were performed at room temperature. The electrochemical cell used for D.C. voltammetry in Ref. [8] was also used for both D.C. and A.C. measurements in the present work to facilitate proper comparison of results from the two sets of studies. This air-tight, small-volume (0.5 ml) glass cell, constructed in the authors' laboratory, used a three-electrode arrangement with a silver wire (2 mm diameter) quasi reference electrode (QRE), and a Pt wire (1 mm diameter) counter electrode coil [8,12,37]. The Ag-QRE helped to avoid undesirable effects of electrolyte contamination and liquid junction potentials [38–41], and its use here was necessitated also by the miniaturized configuration of the experimental cell used [37,42]. This also provided an adequate framework to keep the recorded data, for comparisons as necessary, in the category of the rather vast body of electrochemical results for IL systems reported in the literature using Ag-QREs [40–52]. However, depending on the types and amounts of electro-active species present in the experimental IL, Ag-QREs could sometimes cause drifts in measured potentials [38,39]. Due to this reason, the stability and reproducibility of the voltages measured in this work were checked in separate experiments as noted below.

The Ag-QRE was used as a working electrode in a larger (50 ml) cell, where the open circuit potential (OCP) of this electrode was measured in the experimental IL using a Pt wire QRE, as well as an Ag/Ag^+ reference as described in Ref. [39]. After its initial settlement, the OCP value was repeatable and stable over the time scale of all measurements reported here. In another trial, the Ag wire was placed in a glass frit separator, but no significant changes were observed in the measured potentials. This indicated the absence of potential-altering electro-active species in the system [53]. The thorough Ar-purge of the IL mentioned above also helped to suppress oxide formation on the Ag wire, and contributed further to stabilizing the surface potential of the QRE [8,12].

CV data were collected in the true-analog ramp mode at different voltage scan rates after the OCP was stabilized. Electrochemical windows and sub-windows of the IL–electrode systems were determined using systematic procedure described elsewhere [12]. Experimental (i_r–E) plots were numerically differentiated to determine R from CV. EIS was performed with A.C. perturbation spectra of sine waves having 15 mV amplitude and frequencies in the ranges, 0.01 Hz to 100 kHz, with twenty data points within each logarithmically selected frequency decade of A.C. frequencies. Typically, seven decades of A.C. frequencies were used for EIS, and the recorded spectra were validated through standard Kramers–Kronig (K-K) transform procedures [15]. The K-K analysis ensured the applicability of steady state conditions, reconfirming the absence of any significant effects of possible potential drifts during EIS measurements. In addition, the voltage-dependent EIS data recorded within the electrochemical sub-window were consistent with respect to repeated measurements. ZSimpWin™ was used for CNLS processing of experimental EIS data to obtain EEC models of the electrode-IL interfaces, and the modulus weighting factor was utilized in this step. The parameters selected for recording and ana-

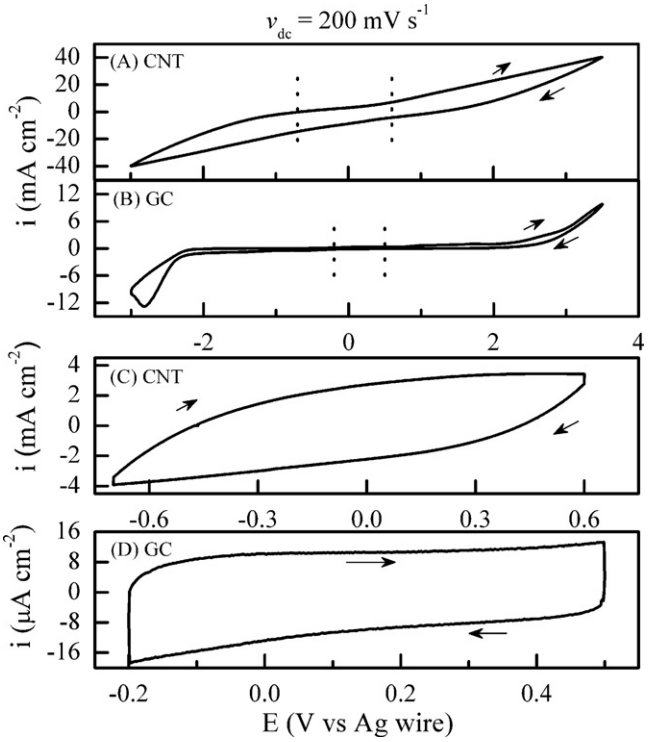

Fig. 2. D.C. CV data for CNT (A and C) and GC (B and D) electrodes, recorded in EMIM-$EtSO_4$ using 200 mV s^{-1} voltage scans in the direction shown by the arrows. (A) and (B) show the full electrochemical windows of CNT and GC, respectively, where the corresponding sub-window regions are indicated by dotted vertical lines. (C) and (D) show voltammograms recorded within these sub-windows. The currents are normalized with respect to the geometric (apparent) surface areas of the electrodes.

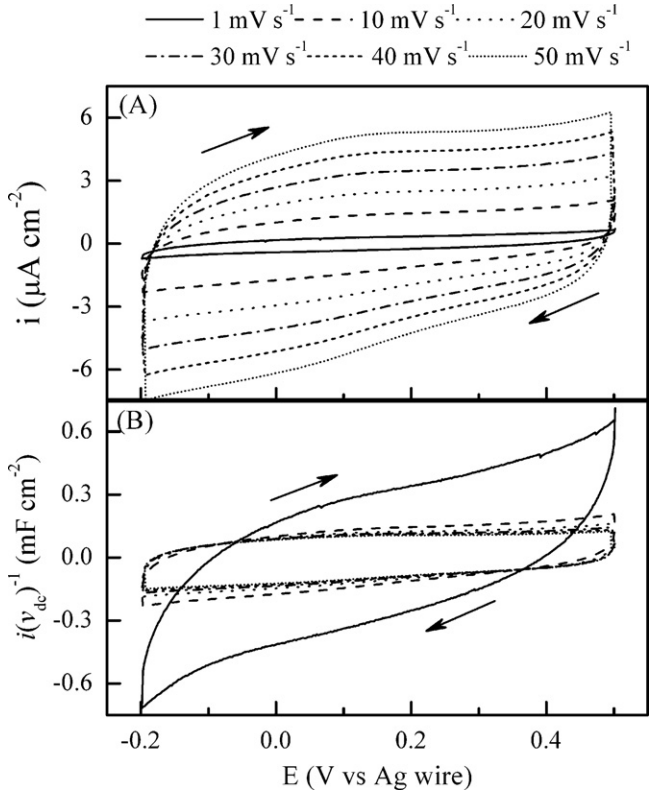

Fig. 3. (A) Cyclic voltammograms for a GC electrode collected at different voltage scan rates (v_{dc} = 1–50 mV s^{-1}) in EMIM-$EtSO_4$ within the electrochemical sub-window of the system. (B) Voltammograms scaled with respect to v_{dc} as a scaling parameter according to Eq. (4).

lyzing the EIS data were optimized through multiple trials to ensure accurate and reproducible results. Trial EECs, based on previously reported studies of similar systems [8,12,21,22] were employed for these calculations, and only those models yielding ≤5% uncertainties in the values of all the circuit elements were accepted. The EEC of Fig. 1C provided satisfactory fits to all the Nyquist spectra recorded for this work. Y_0, n, R_u and R, obtained from these fits were used to determine C_{dl}^{av}.

4. Results and discussion

4.1. Electrochemical windows and sub-windows of EMIM-$EtSO_4$ at the surfaces of CNT and GC electrodes

Cyclic voltammograms indicating the full electrochemical windows of the CNT and GC electrodes in EMIM-$EtSO_4$ are shown in Fig. 2A and B, respectively. The GC surface exhibits distinct faradaic activity at E>2.6 V due to oxidation of $[EtSO_4]^-$, and at E<−2.2 V due to reduction of $[EMIM]^+$ [22,54]. The voltage region between −2.2 and 2.6 V represents the main electrochemical window for GC, where $|i|$<2.5 mA cm^{-2}. The width of this primary voltage window for CNT (from −2.2 to 2.6 V) is comparable to that of GC, but the faradaic features of the currents for CNT are heavily masked by the rather large double layer current of this system. Although the same geometric surface area is utilized for both electrodes, the actual active area of the porous CNT surface is substantially larger than that of the flat GC sample. Thus according to Eq. (2), the larger i_c for CNT is a manifestation of the relatively larger C_{dl} of this electrode.

The electrochemical windows reported here were stable with respect to repeated measurements. Thus, as noted in Section 3, and consistent with previously reported studies [40–44], incorporation of the Ag-QRE in these measurements did not exhibit any significant effects on the potential stability of the system. The potential at the Ag wire QREs is often governed by the solubility and the amount of Ag-complexes present at the surface of the wire [55]. Transient changes in the amount of these Ag-surface species can contribute to potential drifts, and ILs containing Br^- and/or I^- (capable of forming AgBr and AgI complexes onto the Ag-QRE, respectively) appear to be particularly responsive to such effects [55,45]. The Br^- and I^- contents of the IL used in this work were undetectable, with its F^- and Cl^- concentrations at 117 and 404 ppm, respectively [56]. Most probably, the surface chemistry of the Ag-QRE in this case was governed primarily by the Cl^- present in the IL electrolyte, and the concentration of these anions was adequate to prevent potential drifts associated with time dependent depletion of soluble species at the QRE surface [55].

The voltage regions closest to the zero-current-axis, bounded by the vertical dotted lines in Fig. 2A and B, represent the electrochemical "sub-windows" where $|i|$ <5 μA cm^{-2}, and $|i|$<20 μA cm^{-2}, for CNT and GC, respectively. Voltammograms recorded for CNT and GC within these later voltage regions are shown in Fig. 2C and D, respectively. As demonstrated elsewhere [8,12], electrochemical measurements, including those of EIS performed within these sub-windows (−0.7 to 0.6 V for CNT and −0.2 to 0.5 V for GC), are least affected by faradaic oxidation/reduction of the IL ions. Our present study also focuses on the voltage regions of the electrochemical sub-window shown in Fig. 2.

4.2. Sweep rate dependent cyclic voltammetry and separation of faradaic currents from voltammograms

Fig. 3A shows D.C. voltammograms for a GC electrode, collected at different values of v_{dc} in EMIM-$EtSO_4$. The shapes of the voltammograms are similar to those previously reported by other authors

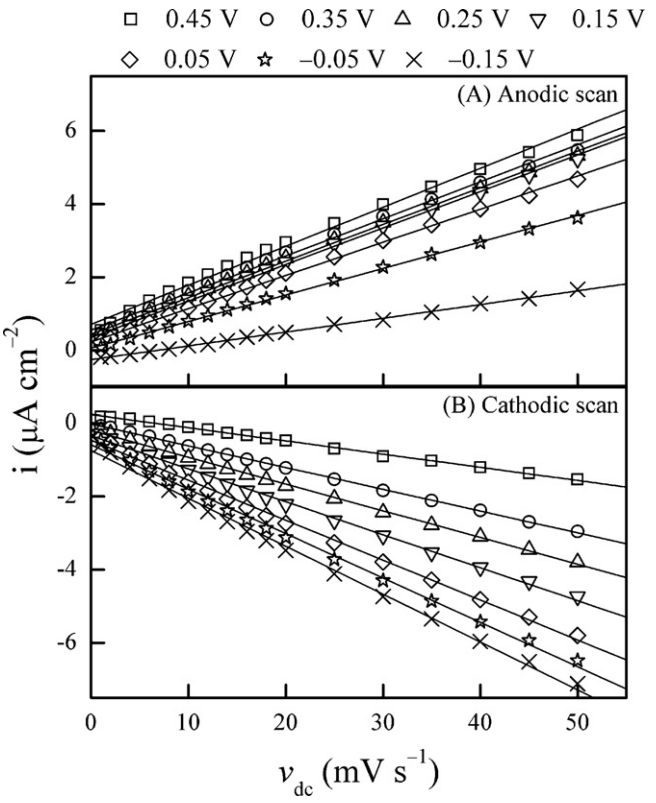

Fig. 4. Electrode currents for GC, recorded using (A) anodic and (B) cathodic CV scans at different values of v_{dc} between 1 and 50 mV s^{-1}. Each plot represents a separate value of E, indicated by different symbols, and the straight lines are fits to the data using Eq. (2). E = 0.45, 0.35, 0.25, 0.15, 0.05, −0.05 and −0.15 V, for the data denoted by the squares, circles, triangles, inverted triangles, diamonds, stars and crosses, respectively.

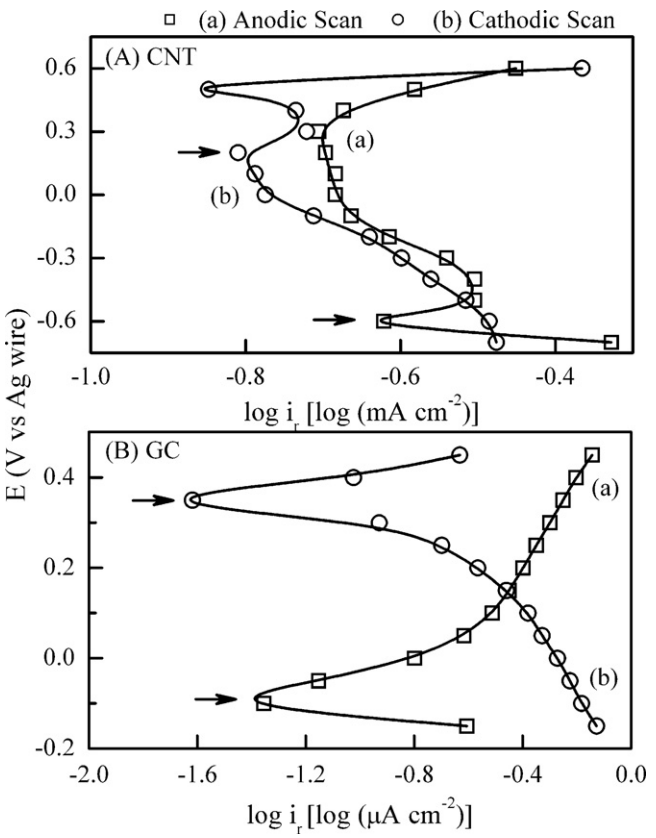

Fig. 5. Tafel-like behaviors of faradaic reaction currents, i_r, for (A) CNT and (B) GC electrodes, measured in a solvent-free electrolyte of EMIM-EtSO$_4$. The symbols represent experimental data, taken from current-axis intercepts of i vs. v_{dc} plots as those shown in Fig. 4. The lines indicate the general trends of the data. In each panel, plots (a) and (b) (squares and circles, respectively) correspond to data recorded using anodic and cathodic CV scans, respectively.

for carbon-based electrodes in different IL electrolytes [57–59]. As the scan speeds are increased, both the anodic and the cathodic currents increase. This observation follows the description of Eq. (2) and implies that the net electrode currents activated by CV are due primarily to charge–discharge of the double layer capacitance ($i \approx i_c$ in Fig. 1B). The plots in Fig. 3B show scaled versions of the data from Fig. 3A using Eq. (4). As v_{dc} is decreased from 50 to 10 mV s^{-1}, starting from the innermost to the sequentially outlying plots in Fig. 3B, the voltammograms gradually expand on both sides of the zero-current-axis. Further reduction of v_{dc} by a full order of magnitude, to 1 mV s^{-1}, significantly enhances this effect as seen in the drastic expansion of the outermost plot in Fig. 3B. This demonstrates that the right hand side of Eq. (4) does not represent C_{dl} in the present case, because this capacitance should be independent of the value of v_{dc}. Results quite similar to those shown here in Fig. 3 were also obtained for the CNT electrode, and have been reported previously [8].

Fig. 4 shows plots of E and v_{dc} dependent electrode currents for the GC electrode activated by (A) positive and (B) negative voltage sweeps of CV. The data points, indicated by different symbols for different values of E, were compiled from Fig. 3A. The lines in Fig. 4 show fits to the data using Eq. (2). The coefficients of determination for all these fits are >0.99, showing close agreement of experimental results with the description of Eq. (2) and Fig. 1C [11]. In particular, the voltage-dependent nonzero plot-intercepts observed on the current-axis of Fig. 4 corroborate the presence of faradaic currents (i_r). A similar analysis has been performed for the CNT electrode in EMIM-EtSO$_4$, and the corresponding results, published previously, also emerged in full agreement with Eq. (2).

The possible origins of the faradaic currents detected for the CNT electrode in EMIM-EtSO$_4$ have previously been discussed in detail [8]. In brief, these currents arise mostly from inherent impurities of the IL and the CNT, and contain both anodic (i_{ra}) and cathodic (i_{rc}) components as noted in Section 2.3 of this report [46,47]. The underlying anodic fardaic reactions of i_{ra} may include oxidation of Fe impurities of CNT by H_2O impurities in the IL as well as oxidation of –COOH groups on the CNT walls. Likewise, the cathodic reactions on CNT may include reduction of functional ketone groups [8]. The GC electrode also contains surface species similar to those formed on CNT [60,61]. Electro-oxidation and -reduction of these reactive surface species under voltage activation of the GC electrode are likely candidates for the faradaic currents (Y-axis intercepts) found here in Fig. 4.

Since i_r emerges here from a linear dependence of i on v_{dc} (that is, i not being proportional to $\sqrt{v_{dc}}$), this reaction current is not diffusion controlled [62]. To check the voltage dependence of this kinetically controlled i_r, we plot log $|i_r|$ against E for the CNT and the GC electrodes in Fig. 5A and B, respectively. The symbols in these plots are data points and the lines are included to guide the eye. The plots for GC in Fig. 5B show strong Tafel-like characteristics that are signature attributes of Butler–Volmer kinetics [62]. This Tafel behavior of i_r is relatively less prominent in Fig. 5B due to multiple voltage-dependent current features observed there. Nevertheless, the features of i_r observed in Fig. 5A at −0.4 V (for anodic scan in plot (a)) and at 0.4 V (for cathodic scan in plot (b)) are typical of surface passivation reactions in the description of Butler–Volmer kinetics [63]. The increases in i_r with increasing voltages at 0.3 V (for anodic scan in plot (a)) and at 0.5 V (for

cathodic scan in plot (b)) can be attributed to voltage induced breakdown of surface passivation films formed at lower voltages [63]. These passivation/de-passivation currents in Fig. 5B most likely are associated with the formation and subsequent collapse of site-blocking $Fe(OH)_2$ films. These passive films can appear due to anodic reactions between the Fe impurities of CNT and residual traces of water in the IL: $Fe + 2H_2O = Fe(OH)_2 + 2H^+ + 2e^-$ [8].

Thus, the CNT and GC electrodes in EMIM-$EtSO_4$ seem to support faradaic side reactions that are characterized by Butler–Volmer kinetics. These observations are consistent with those of Taylor et al. who recently reported evidence for Butler–Volmer features of heterogeneous electron transfer at an IL–Pt interface [64]. The voltages corresponding to the horizontal arrows in Fig. 5, where the main cathodic and anodic current branches meet, can be taken as equilibrium- or corrosion-potentials [63] of the systems studied. For both electrodes, this potential shifts to higher voltages in going from the anodic to the cathodic scan. This effect is typical of reactions generating surface-blocking species during voltage scans [12,67], and is frequently observed in CV studies of metal electrodes in aqueous electrolytes [65,66]. Furthermore, time-domain response of the distributed double layer capacitance can cause a measurable hysteresis between the anodic and cathodic currents in CV as voltage scan speeds are increased [32,33]. This also can introduce different voltage dependencies in the faradaic currents generated with positive and negative voltage sweeps, as exhibited by the mutually displaced positions of plots (a) and (b) in both panels of Fig. 5.

4.3. Electrochemical impedance results for CNT and GC electrodes in [EMIM-$EtSO_4$]

Impedance spectra for the CNT and GC electrodes were collected at several D.C. bias voltages within the respective electrochemical sub-windows of these electrodes. Sample Nyquist plots from these EIS experiments are shown in Fig. 6, where Z' and Z'' are the real and imaginary parts of Z, respectively. The lines represent CNLS fits to experimental data (symbols) using the EEC of Fig. 1C. Attempts of fitting the data using Fig. 1A resulted in large errors in the calculated impedance elements, confirming that the assumption of a simple IPE was inapplicable to the presently used IL–electrode interfaces.

The values of Z' and Z'' for GC (in Fig. 6B) are larger than those of CNT (in Fig. 6A), consistent with the relatively lower D.C. currents observed for GC in Fig. 2. Although the GC electrode is substantially more flat compared to the CNT electrode, the microscopic surface in-homogeneity of the former [60] still is manifested in its CPE behavior observed here (Fig. 1C). The plot-intercepts on the high-frequency end of the Z' axis in Fig. 6 correspond to R_u, which essentially is voltage independent, with average values of 39.0 and 13.5 $\Omega\,cm^2$ for the CNT and GC electrodes, respectively. All impedance parameters were normalized with respect to the geometric apparent electrode areas and the relatively larger electrolyte resistance found for the CNT system was a result of the considerably larger actual area of its porous surface.

Fig. 7 shows voltage sensitive variations of the CPE parameters (a) n and (b) Y_0, obtained from CNLS fits to experimental Nyquist plots for the (A) CNT and (B) GC electrodes. The inequality, $n \geq 0.98$, is sometimes used as an empirical condition necessary to reasonably approximate a CPE as a capacitance [11]. For the CNT electrode, the values of n fall below this critical value throughout the experimental voltage range. Therefore, even from empirical considerations, Y_0 for CNT cannot be characterized here as a double layer capacitance. For the GC electrode also, the observed values of n mostly are below 0.98, implying that Y_0 in Fig. 7B cannot be approximated as the double layer capacitance [11–13]. The observed voltage-dependent variations of n are caused by corresponding changes in electrode surface morphologies [10,24]. For GC, these changes

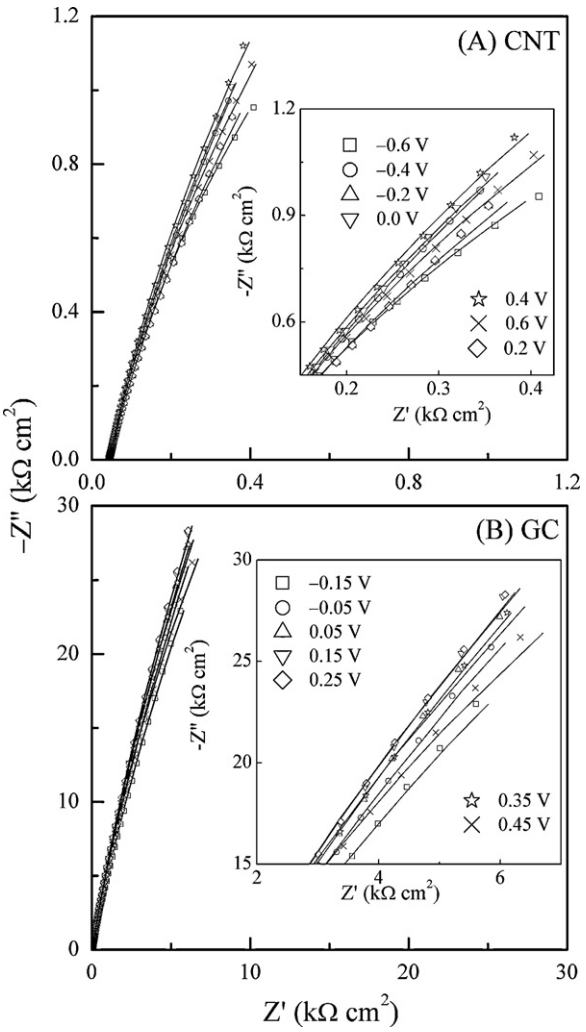

Fig. 6. Elucidatory Nyquist plots for (A) CNT and (B) GC electrodes in EMIM-$EtSO_4$. The insets show magnified views of the low-frequency regions of the Nyquist spectra. The different symbols correspond to experimental data recorded at different D.C. voltages as noted in the insets. The lines represent CNLS fits to the data using the circuit model shown in Fig. 1C.

are relatively more gradual, consistent with the rather clearly pronounced Butler-Volmer kinetics found for this electrode in Fig. 5A. On the other hand, the passivation features of CNT noted in Fig. 5B complicate the detailed voltage-dependent surface structure of this electrode. The observed voltage dependencies of Y_0 in Fig. 7 are caused by those of its constituent parameter(s) R (and possibly C_{dl}^{av}) [14].

According to Eq. (15), Z'' initially increases with decreasing values of ω, and after reaching a maximum value, returns to zero as $\omega \to 0$ when Z becomes real and equal to $(R_u + R)$ [10,14]. The insets in Fig. 6 show how the lower-frequency regions of the Nyquist plots tend to separate as the regions of maximum Z'' are approached. These plots indicate that the maximum of Z'' has not been reached within the low-frequency limit used for EIS. This is expected whenever the polarization resistance is very large [10,59], and as shown below the presently used systems are indeed associated with such large values of R.

4.4. Polarization resistances obtained using CV and EIS techniques

Voltage-dependent polarization resistances for the (A) CNT and (B) GC electrodes, obtained from (a) CV and (b) EIS measurements are compared in Fig. 8. To get R from CV, both the anodic and

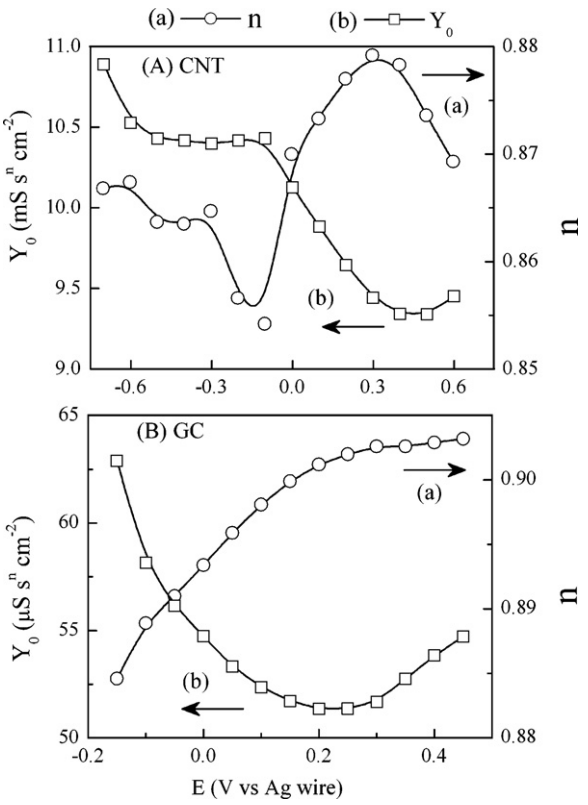

Fig. 7. D.C. voltage-dependent variations of the CPE parameters n (plots (a), right vertical axis) and Y_0 (plots (b), left vertical axis) obtained from CNLS analyses of experimental Nyquist plots for (A) CNT and (B) GC electrodes recorded in EMIM-$EtSO_4$. The lines through the data points represent the overall trend of the data.

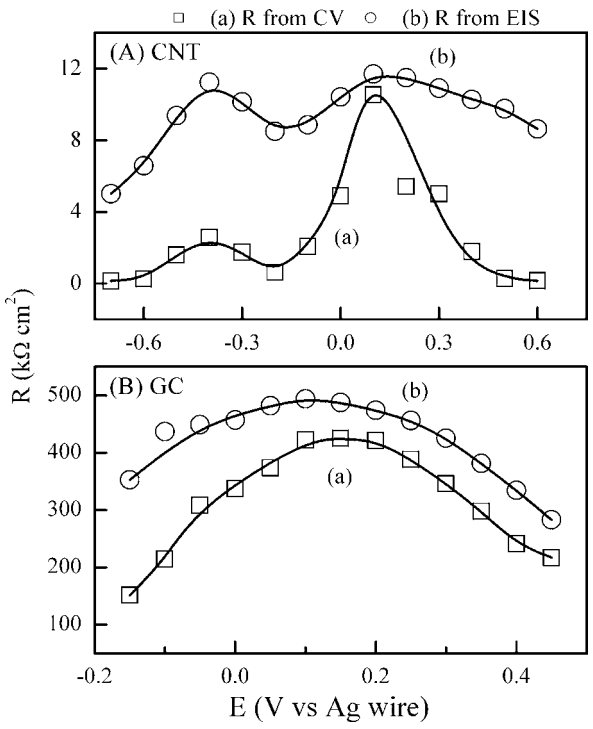

Fig. 8. Polarization resistances R, measured with CV (plots (a)) and EIS (plots (b)) for CNT (panel A) and GC (panel B) electrodes in EMIM-$EtSO_4$. The symbols are experimental data, and the lines indicate the overall voltage-dependent inclinations of the data.

the cathodic sides of i_r vs. E were numerically differentiated to obtain $|\partial i_r/dE|^{-1}$. For each electrode, the resulting data points in the anodic branch lying above the equilibrium potential were taken as the anodic component, R_a, of the polarization resistance. Similarly, the $|\partial i_r/dE|^{-1}$ data-segment from the cathodic branch lying below the corresponding equilibrium potential was taken as the cathodic polarization resistance R_c. Plots (a) in Fig. 8 represent the net polarization resistance, $R = [(1/R_a) + (1/R_c)]^{-1}$, evaluated from these CV data. Plots (b) in Fig. 8 show R obtained directly from CNLS-analyzed EIS data.

For both electrodes considered in Fig. 8, the general voltage-dependent features of R are comparable between the CV and EIS results. Usually, R increases with reduced electrode reactivity at voltages corresponding to D.C. equilibrium and surface passivation [50,52,53]. For GC in Fig. 8B, a broader peak-like feature of R is observed between 0.1 and 0.2 V of both plots (a) and (b). This region corresponds to the average of the D.C. equilibrium potentials indicated by plots (a) and (b) in Fig. 5. For CNT, R in Fig. 8A has two relatively wide peaks around 0.1 and −0.4 V, and these voltages are associated with the equilibrium and passivation conditions for this electrode as indicated by plots (b) and (a) in Fig. 5A, respectively.

Despite the overall similarities found between the CV and EIS data in Fig. 8, the detailed voltage controlled values of R are noticeably different between the two sets of measurements. To a large extent, these differences can be attributed to different levels of surface reactivity supported by the measurement conditions of the two techniques [66]. The control variables used in CV and EIS can also affect the measurement of R [10,30,31,67] and these effects are particularly strong in EIS sampling of systems exhibiting CPE characteristics. As pointed out by Zoltowski, for CPE systems containing finite polarization resistances, the measured EEC elements can be sensitive to a number of factors including the A.C. frequency range applied, number of data points recorded per frequency decade, and the weighting scheme used for CNLS calculations [13]. The systems studied here fall under this category. Another relevant point to be noted here is that, voltage dependence of R is not specifically accounted for in the derivation of Eq. (8). Since this equation forms the basis for measuring R (as a function of E) using EIS, it is difficult to quantitatively compare the CV- and EIS-based R–E profiles obtained in the phenomenological approach using Fig. 1B and C.

The arc-like graphs of Fig. 6 would eventually become a complete loop as $\omega \to \infty$ when $Z' \to (R_u + R)$ and $Z'' \to 0$ at [10]. On the Nyquist graph, this point of coordinate $(R_u+R,0)$ resides far to the right of the highest value of Z' monitored at the lowest frequencies used here, as indicated by the low-frequency ends of the Nyquist plots pointing away from the Z' axis in Fig. 6. Plot (b) in Fig. 8 represents CNLS-calculated values of R corresponding to these extrapolated coordinates $(R_u + R_u,0)$ on the experimental Nyquist plots. Thus, all the values of R in Fig. 8 are considerably larger than the maximum Z' values measured in the Nyquist plots for the corresponding systems in Fig. 6. These large polarization resistances indicate that their associated faradaic reactions are weak, but still are readily detectable in EIS.

4.5. Double layer capacitances obtained using CV and EIS techniques

Fig. 9 shows (a) C_{dl} and (b) C_{dl}^{av}, determined using CV and EIS, respectively, for the (A) CNT (B) GC electrodes in EMIM-$EtSO_4$. In the case of CV, the scaled capacitance C'_{dl} was determined for both anodic and cathodic voltage scans in terms of the slopes of linear $(i - v_{dc})$ plots like those shown in Fig. 4 here and in Fig. 5 of Ref. [8]. Values of R measured using CV (plots (a) and (b) of Fig. 7) and those of R_u determined using EIS were utilized to calculate C_{dl} from C'_{dl}. Results obtained in this way from anodic and cathodic CV scans were averaged to arrive at the final plots (a) shown in Fig. 9. The graphs of C_{dl}^{av} in Fig. 9 were obtained by combining the EIS-

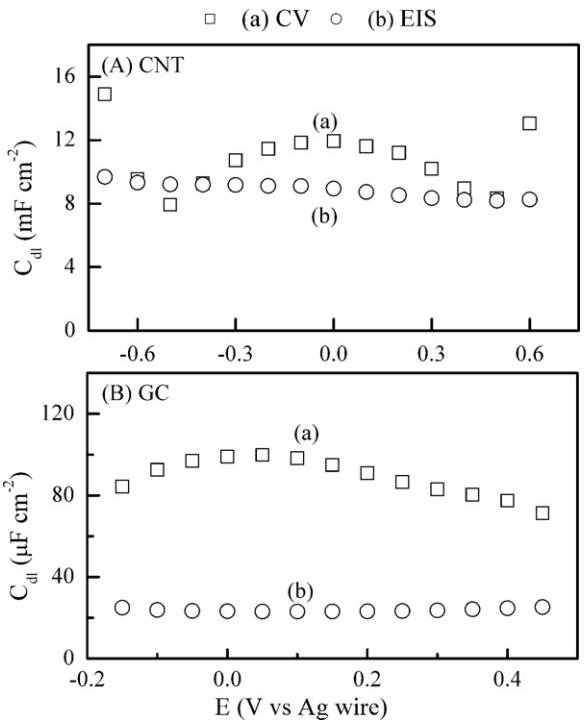

Fig. 9. Voltage-dependent double layer capacitance values, determined using CV (C_{dl} in plots (a)) and EIS (C_{dl}^{av} in plots (b)) for (A) CNT and (B) GC electrodes in EMIM-EtSO$_4$. The CV data represent average of C_{dl} values obtained using positive and negative voltage scans.

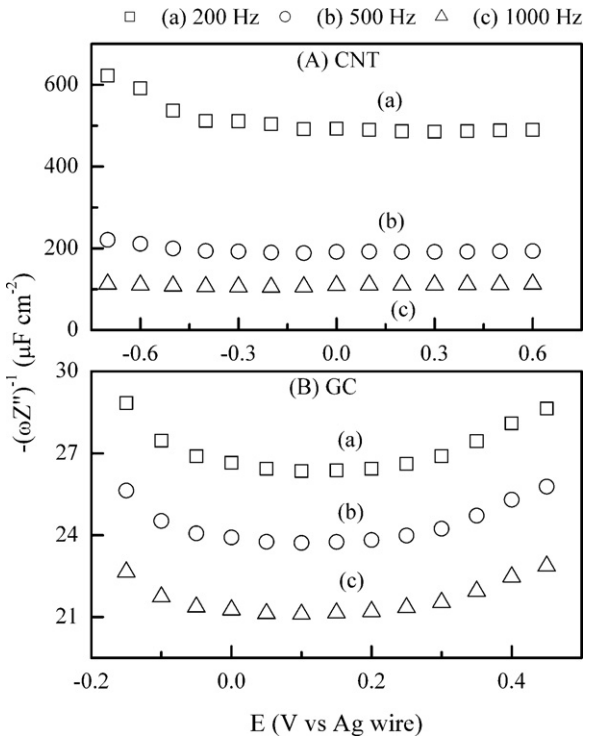

Fig. 10. Voltage-dependent values of the term $-(\omega Z'')^{-1}$, defined in Eq. (16), for (A) CNT and (B) GC electrodes in EMIM-EtSO$_4$, obtained through single-frequency impedance measurements at selected frequencies ($f = [\omega/2\pi]$) of the A.C. perturbation voltage.

measured values of Y_0 (Fig. 7), R (plots (b) in Fig. 8) and R_u in Eq. (14). The capacitance values for CNT came out at least two orders of magnitude larger than those of GC, indicating the highly porous nature of the former electrode [3–5]. Fig. 9 also suggests that the double layer capacitances of the IL–carbon interfaces studied here are relatively insensitive to voltage variations within the electrochemical sub-windows used. This observation is in full agreement with previously reported results for similar systems [4,59,68].

In Fig. 9A, the overall values of C_{dl} and C_{dl}^{av} are comparable, although the detailed voltage dependencies of the two parameters are somewhat different. These latter differences could be associated with the different response characteristics of Q_{dl} to the frequency and time-domain measurements in EIS and CV, respectively [10,23,32,33]. At −0.7 and 0.6 V, the C_{dl} values for CNT show significant departure from those of the corresponding C_{dl}^{av}. This is expected, since these latter voltages correspond to the outer bounds of the electrochemical sub-window, where the CV characteristics of the CNT electrode tend to deviate from the description of Eq. (2) [8].

For GC in Fig. 9B, C_{dl} and C_{dl}^{av} display mutually comparable orders of magnitudes, but their values are noticeably different. The factors responsible for these differences are the same as those discussed in the context of Fig. 8 to explain the CV- and EIS-measured values. In Fig. 9, C_{dl} and C_{dl}^{av} for CNT are in closer mutual agreement in comparison with those for GC. This observation suggests that the assumptions leading to Eq. (14) for EIS-based measurement of C_{dl}^{av} may be applicable in varied degrees to different experimental systems. Brug et al. also have explicitly noted the simplistic nature of the un-branched ladder-EEC model used to derive Eq. (11) [14]. At the same time, as discussed in our earlier work, the analysis of C_{dl} using the CV formalism of Eq. (2) also is based on certain assumptions that might depend on various system-specific experimental details. Thus, depending on the IL–electrode interfaces used, and the procedures adapted for data analysis, CV- and EIS-measured double layer capacitances for such systems may show detectably different results [10,13,23,32,33]. As demonstrated in the present work, faradaic reactions and electrode-surface in-homogeneities are likely to play critical roles in causing these differences.

It is also demonstrated here that combining CV with EIS could be useful to probe double layer capacitances of IL–carbon systems displaying CPE behaviors. Results of CV and EIS found in mutual agreement should be most reliable in this regard (Fig. 9A). If the results found from the two techniques are not fully coincident, in many cases (e.g. in Fig. 9B), the CV results can be used as a primary reference, since data-processing in this approach does not strictly require an additional model to describe the (often system-specific) site-distributed impedance elements. In addition, all the D.C. data necessary to calculate the double layer capacitance, as well as those necessary to analyze the faradaic response of the system (Figs. 4 and 5 and plots (a) in Figs. 8 and 9) come from just differently processed forms of results obtained from a given set of CV experiments (Fig. 3A). This approach also helps to minimize experimental uncertainties, especially those associated with long term potential stabilities.

4.6. Considerations for differential capacitances measurements using the single-frequency impedance method

The working principle of these approaches based on Eq. (17), and the general experimental constraints of such measurements have been discussed elsewhere in detail [28]. A series of experiments were carried out in the present work to examine if this technique would be suitable for studying the electrochemical systems considered here. The A.C. perturbation frequencies most commonly reported for these studies vary between 200 and 1000 Hz [34–36]. Therefore, our measurements also were performed exploring this specific frequency range and the corresponding results for the (A) CNT and (B) GC electrodes are shown in Fig. 10. The plots show voltage-dependent values of the

right hand side of Eq. (17) (which also is the left hand side of Eq. (16)), evaluated using experimentally measured Z'' at selected frequencies.

The parameter $-(1/\omega Z'')$ plotted in Fig. 10 is strongly frequency dependent and disagree with both sets of the C_{dl} and C_{dl}^{av} data shown in Fig. 9. This is expected, because Eq. (17) is only valid for $n \to 1$ and $R \to \infty$, whereas Figs. 7 and 8 show that neither of these criteria is met here. Thus, the quantity plotted in Fig. 10 represents the full expression shown on the right hand side of Eq. (16), which depends both on voltage variations (in a complex manner [13–15], through those of R and Y_0) and on the value of ω. These plots do not represent the double layer capacitances of the electrochemical interfaces studied here. We also note in this context that for predominantly capacitive interfaces involving aqueous electrolytes, a capacitance minimum on the voltage axis usually represents the potential of zero charge (PZC) [9,62]. Some features resembling such minimum points are seen in Fig. 10B, but due to the reasons discussed above these features cannot be associated with the PZC. Recently, Gnahm et al. also have reported similar observations regarding the implications of capacitance minima for IL based systems [68].

5. Conclusions

The analytical capabilities of the CV and EIS techniques have been combined in this work to measure double layer capacitances of CNT and GC electrodes in a solvent-free IL of EMIM-$EtSO_4$. The results suggest that in the analysis of experimental data for such systems, it is necessary to adequately account for (i) residual faradaic reactions, and (ii) spatial in-homogeneity of the electrode interfaces. Both the carbon electrodes studied here exhibited faradaic side reactions within their electrochemical sub-windows. The faradaic currents extracted from voltage scan rate dependent cyclic voltammograms displayed Tafel-like features, and provided a D.C. measure of the polarization resistance. EIS confirmed the presence of these faradaic processes and also demonstrated how inhomogeneous surface morphologies of the electrodes could affect capacitance measurements in the A.C. approach. The overall features and magnitudes of polarization resistances measured with EIS were comparable to those determined using CV.

The double layer capacitance of the porous CNT electrode has been found to be about three orders of magnitude larger than that of the flat GC sample. Certain system-specific differences have been detected between the capacitance values measured using CV and EIS. The underlying factors contributing to these differences appeared to be associated in part with the assumptions of the model used to extract double layer capacitance values from the CPE parameters. The utility of the fixed-frequency impedance technique also was tested using the same IL–electrode systems. These latter measurements resulted in considerably frequency-dispersed values of the capacitance-like term $-(\omega Z'')^{-1}$ that were in significant disagreement with the frequency-independent capacitances found from CV and EIS. The results reported here underscore the importance of adapting a generalized framework for data analysis that extends beyond the considerations of ideally polarized homogeneous electrodes. The analytical approach adapted here using CV and EIS demonstrates certain essential elements of such a generalized framework by including the effects of solution resistance, faradaic side reactions, and electrode-surface in-homogeneity. This strategy for combining CV and EIS can easily be extended to carry out detailed studies of other IL–electrode systems.

Acknowledgement

This work was supported by the Army Research Office (grant no. W911NF-05-1-0339).

References

[1] C. Arbizzani, M. Biso, D. Cericola, M. Lazzari, F. Soavi, M. Mastragostino, J. Power Sources 185 (2008) 1575–1579.
[2] W. Lu, L. Qu, K. Henry, L. Dai, J. Power Sources 189 (2009) 1270–1277.
[3] V.V.N. Obreja, Physica E 40 (2008) 2596–2605.
[4] E. Frackowiak, J. Braz. Chem. Soc. 17 (2006) 1074–1082.
[5] M. Ue, Application of ionic liquids to double-layer capacitors, in: H. Ono (Ed.), Electrochemical Aspects of Ionic Liquids, Wiley, New York, 2005, pp. 205–223.
[6] A.A. Kornyshev, J. Phys. Chem. B 111 (2007) 5545–5557.
[7] K.B. Oldham, J. Electroanal. Chem. 613 (2008) 131–138.
[8] J.P. Zheng, C.M. Pettit, P.C. Goonetilleke, G.M. Zenger, D. Roy, Talanta 78 (2009) 1056–1062.
[9] M. Sluyters-Rehbach, Pure Appl. Chem. 66 (1994) 1831–1891.
[10] E. Barsoukov, J.R. Macdonald (Eds.), Impedance Spectroscopy, Wiley, New York, 2005.
[11] A. Sadkowski, J. Electroanal. Chem. 481 (2000) 232–236.
[12] S.S. Moganty, R.E. Baltus, D. Roy, Chem. Phys. Lett. 483 (2009) 90–94.
[13] P. Zoltowski, J. Electroanal. Chem. 443 (1998) 149–154.
[14] G.J. Brug, A.L.G. van Eeden, M. Sluyters- Rehbach, J. Sluyters, J. Electroanal. Chem. 176 (1984) 275–295.
[15] V.M. Huang, V. Vivier, M.E. Orazem, N. Pébère, B. Tribollet, J. Electrochem. Soc. 154 (2007) C99–C107.
[16] A. Lewandowski, M. Galinski, J. Power Sources 173 (2007) 822–828.
[17] F. Soavi, M. Mastragostino, J. Power Sources 185 (2008) 1575–1579.
[18] A. Burke, J. Power Sources 91 (2000) 37–50.
[19] J.-C. Lasdguès, J. Grondin, T. Becker, L. Servant, M. Hernandez, Solid State Ionics 77 (1995) 311–317.
[20] S. Åberg, J. Electroanal. Chem. 419 (1997) 99–103.
[21] F. Silva, C. Gomes, M. Figueiredo, R. Costa, A. Martins, C.M. Pereira, J. Electroanal. Chem. 622 (2008) 153–160.
[22] J.N. Barisci, G.G. Wallace, D. Chattopadhyay, F. Papadimitrakopoulos, R.H. Baughman, J. Electrochem. Soc. 150 (2003) E409–E415.
[23] T. Pajkossy, Solid State Ionics 176 (2005) 1997–2003.
[24] U. Rammelt, G. Reinhard, Electrochim. Acta 35 (1990) 1045–1049.
[25] P.S. Germain, W.G. Pell, B.E. Conway, Electrochim. Acta 49 (2004) 1775–1788.
[26] Y. Zhou, B. He, W. Zhou, J. Huang, X. Li, B. Wu, H. Li, Electrochim. Acta 49 (2004) 257–262.
[27] H.A. Andreas, B.E. Conway, Electrochim. Acta 51 (2006) 6510–6520.
[28] C.M. Pettit, P.C. Goonetilleke, D. Roy, J. Electroanal. Chem. 589 (2006) 219–231.
[29] C.M. Pettit, P.C. Goonetilleke, C.M. Sulyma, D. Roy, Anal. Chem. 78 (2006) 3723–3729.
[30] D.D. Macdonald, J. Electrochem. Soc. 125 (1978) 1443–1449.
[31] E.G. Gagnon, J. Electrochem. Soc. 121 (1974) 512–515.
[32] A. Sadkowski, Electrochim. Acta 38 (1993) 2051–2054.
[33] G. Lee, S. Pyun, Electrochim. Acta 51 (2006) 3029–3038.
[34] V. Lockett, R. Sedev, J. Ralston, M. Horne, T. Rodopoulos, J. Phys. Chem. C 112 (2008) 7486–7495.
[35] Md.T. Alam, M.M. Islam, T. Okajima, T. Ohsaka, J. Phys. Chem. C 112 (2008) 2601–2606.
[36] Md.M. Islam, M.T. Alam, T. Ohsaka, J. Phys. Chem. C 112 (2008) 16568–16574.
[37] P.C. Goonetilleke, Ph.D. Thesis, Clarkson University, Potsdam, 2008.
[38] J. Ghilane, P. Hapiot, A.J. Bard, Anal. Chem. 78 (2006) 6868–6872.
[39] A. Saheb, J. Janata, M. Josowicz, Electroanalysis 18 (2006) 405–409.
[40] M.C. Buzzeo, C. Hardacre, R.G. Compton, Chem. Phys. Chem. 7 (2006) 176–180.
[41] E.I. Rogers, D.S. Silvester, D.L. Poole, L. Aldous, C. Hardacre, R.G. Compton, J. Phys. Chem. C 112 (2008) 2729–2735.
[42] U. Guth, F. Gerlach, M. Decker, W. Oelbner, W. Vonau, J. Solid State Electrochem. 13 (2009) 27–39.
[43] F. Endres, D. MacFarlane, A. Abbott (Eds.), Electrodeposition from Ionic Liquids, Wiley-VCH, Weinheim, 2008.
[44] G.H. Min, T. Yim, H.Y. Lee, D.H. Huh, E. Lee, J. Mun, S.M. Oh, Y.G. Kim, Bull. Korean Chem. Soc. 27 (2006) 847–852.
[45] D.S. Silvester, T.L. Broder, L. Aldous, C. Hardacre, A. Crossley, R.G. Compton, Analyst 132 (2007) 196–198.
[46] T. Devarajan, S. Higashiya, C. Dangler, M. Rane-Fondacaro, J. Snyder, P. Haldar, Electrochem. Commun. 11 (2009) 680–683.
[47] A.P. Abbott, K. El-Taib, K.S. Ryder, E.L. Smith, Trans. Inst. Metal Finish. 86 (2008) 234–240.
[48] A.I. Bhatt, A.M. Bond, J. Electroanal. Chem. 619–620 (2008) 1–10.
[49] D.L. Boxall, J.J. O'Dea, R.A. Osteryoung, J. Electrochem. Soc. 149 (2002) E468–E471.
[50] L. Wen, I.D. Norris, B.R. Mattes, Austr. J. Chem. 58 (2005) 263–269.
[51] Z. Li, I. Pobelov, B. Han, T. Wandlowski, A. Błaszczyk, M. Mayor, Nanotechnology 18 (2007) 044018–044025.
[52] S. Baldelli, J. Phys. Chem. B 109 (2005) 13049–13051.
[53] V.M. Hultgren, A.W.A. Mariotti, A.M. Bond, A.G. Wedd, Anal. Chem. 74 (2002) 3151–3156.
[54] J. Xie, T.L. Riechel, J. Electrochem. Soc. 145 (1998) 2660–2664.
[55] G.A. Snook, A.S. Best, A.G. Pandolfo, A.F. Hollenkamp, Electrochem. Commun. 8 (2006) 1405–1411.
[56] Material Safety Data Sheet for ECOENG™ 212, Solvent Innovations, Cologne, 2004.
[57] M. Lazzari, M. Mastragostino, F. Soavi, Electrochem. Commun. 9 (2007) 1567–1572.

[58] A.B. Fuertes, G. Lota, T.A. Centeno, E. Frackowiak, Electrochim. Acta 50 (2005) 2799–2805.
[59] B. Xu, F. Wu, R. Chen, G. Cao, S. Chen, Z. Zhou, Y. Yang, Electrochem. Commun. 10 (2008) 795–797.
[60] S. Ranganathan, T.C. Kuo, R.L. McCreery, Anal. Chem. 71 (1999) 3574–3580.
[61] P. Chen, R.L. McCreery, Anal. Chem. 68 (1996) 3958–3965.
[62] A.J. Bard, L.R. Faulkner, Electrochemical Methods, second ed., Wiley, New York, 2001.
[63] M.G. Fontana, Corrosion Engineering, McGraw Hill, New York, 1986.
[64] W. Taylor, F. Qiu, J. Hu, P. Licence, D.A. Walsh, J. Phys. Chem. B 112 (2008) 13292–13299.
[65] J.P. Zheng, D. Roy, Thin Solid Films 517 (2009) 4587–4592.
[66] C.M. Sulyma, D. Roy, Appl. Surf. Sci. 256 (2010) 2583–2595.
[67] P. Hapiot, C. Lagrost, Chem. Rev. 108 (2008) 2238–2264.
[68] M. Gnahm, T. Pajkossy, D.M. Kolb, Electrochim. Acta (2010), doi:10.1016/j.electacta.2009.08.031.